

Pattern-induced anchoring transitions in nematic liquid crystals

Óscar A. Rojas-Gómez

Departamento de Física Atómica, Molecular y Nuclear, Area de Física Teórica, Universidad de Sevilla, Apartado de Correos 1065, 41080 Sevilla, Spain

José M. Romero-Enrique

Departamento de Física Atómica, Molecular y Nuclear, Area de Física Teórica, Universidad de Sevilla, Apartado de Correos 1065, 41080 Sevilla, Spain

Nuno M. Silvestre

Departamento de Física e Centro de Física Teórica e Computacional, Faculdade de Ciências, Universidade de Lisboa, Campo Grande, P-1749-016, Lisbon, Portugal

Margarida M. Telo da Gama

Departamento de Física e Centro de Física Teórica e Computacional, Faculdade de Ciências, Universidade de Lisboa, Campo Grande, P-1749-016, Lisbon, Portugal

Abstract. In this paper we revisit the problem of a nematic liquid crystal in contact with patterned substrates. The substrate is modelled as a periodic array of parallel infinite grooves of well-defined cross section sculpted on a chemically homogeneous substrate which favors local homeotropic anchoring of the nematic. We consider three cases: a sawtooth, a crenellated and a sinusoidal substrate. We analyse this problem within the modified Frank-Oseen formalism. We argue that, for substrate periodicities much larger than the extrapolation length, the existence of different nematic textures with distinct far-field orientations, as well as the anchoring transitions between them, are associated with the presence of topological defects either on or close to the substrate. For the sawtooth and sinusoidal case, we observe a homeotropic to planar anchoring transition as the substrate roughness is increased. On the other hand, a homeotropic to oblique anchoring transition is observed for crenellated substrates. In this case, the anchoring phase diagram shows a complex dependence on the substrate roughness and substrate anchoring strength.

1. Introduction

In the last decades the study of nematic liquid crystals in the presence of microstructured substrates has been the subject of intense research [1–3]. This problem is interesting not only from a fundamental point of view, but also due to its practical applications, such as the design of zenithally bistable devices [4–9], or the trapping of colloidal particles on specified sites [10–14]. The presence of the structured substrate typically distorts the nematic orientational order, leading to elastic distortions and the formation of topological defects. On the other hand, the substrate topography can determine the director orientation far away from the substrate. Since the seminal work of Berreman [15, 16], this problem has been extensively studied and generalized in the literature [4, 17–34]. Wetting and filling transitions by nematics on these surfaces have also been studied [35–40]. When the substrate has cusps, disclination-like singularities generally appear at or very close to them [17–19, 30–32, 41]. However, even when the substrate is smooth disclination lines may appear, in the nematic, close to the substrate [33, 34, 38]. In both cases, these orientation-field singularities play an important role to understand the different textures of the nematic in contact with a patterned substrate under strong anchoring conditions.

In this paper we investigate the equilibrium nematic texture at substrates of arbitrary cross section, and determine how this texture determines the (homogeneous) nematic director in the far-field. Anchoring transitions are identified as the transitions between nematic textures with different far-field orientations. We will assume that the nematic director field lies in the plane perpendicular to the patterned substrate longitudinal axis, and that the substrate lengthscales are large enough to ensure strong anchoring conditions on the substrate. In a few cases analytical results are available [17, 29, 32, 34, 41, 42], but in general we have to resort to numerical methods.

Most studies involve numerical minimization of free-energy functionals such as the Landau-de Gennes or Frank-Oseen models. The Landau-de Gennes model describes the emergence of topological defects, but it is very time-consuming and it is difficult to obtain systematic results when the pattern length scales are much larger than the nematic coherence length. On the other hand, in the Frank-Oseen model topological defects need to be included by hand.

In Ref. [32] we extended the Frank-Oseen model to include disclination-like singularities near the cusps of a sawtooth substrate, and found excellent agreement with previous Landau-de Gennes calculations [31]. In this paper we generalize this numerical method to surface reliefs of arbitrary sections (with or without cusps), as well as in the presence of disclination lines in the nematic phase. We apply our method to study the anchoring transitions induced by the patterned substrate in sawtooth, crenellated and sinusoidal substrates under strong anchoring conditions.

The paper is organized as follows. In section 2 is devoted we set the problem. The numerical technique is presented in Section 3. Results on sawtooth, crenellated and sinusoidal substrates are discussed in Section 4. Finally, we end with the conclusions

in Section 5. Technical details of the numerical method and of the analytic solution of the free-energy elastic contribution for a particular nematic texture on crenellated substrates are described in the appendix.

2. The model

We consider a nematic liquid in contact with a patterned substrate with a relief profile $\psi(x, z)$ that favours local homeotropic anchoring of the molecules (see Fig. 1). Translational symmetry along the z axis is assumed, so that $\psi = \psi(x)$. On the other hand, the substrate is periodic along the x -axis with a wavelength λ , i.e. $\psi(x+\lambda) = \psi(x)$. Furthermore, we assume that the nematic director field $\mathbf{n}(\mathbf{r})$ exhibits only in-plane distortions, and thus it can be parametrized by the angle θ between the local director and the y axis, yielding $\mathbf{n}(\mathbf{r}) = (-\sin\theta(\mathbf{r}), \cos\theta(\mathbf{r}), 0)$. The nematic order may be represented locally by a traceless symmetric second-rank tensor order parameter \mathbf{Q} , with Cartesian components $Q_{ij} = \frac{3}{2}S[n_i n_j - \frac{1}{3}\delta_{ij}] + \frac{1}{2}B[l_i l_j - m_i m_j]$, where S is the nematic order parameter, which measures the orientational ordering along the nematic director, and B the biaxiality order parameter, which measures the ordering of the molecules along directions perpendicular to \mathbf{n} , characterized by the eigenvectors \mathbf{l} and \mathbf{m} . We consider uniaxial nematic liquid crystals, so that $B = 0$ except close to the substrate or within the topological defect cores. Note that an inversion of \mathbf{n} does not change the value of \mathbf{Q} , and thus in nematics, \mathbf{n} and $-\mathbf{n}$ are physically equivalent configurations.

Far from the substrate, no specific orientation is imposed, but we require that the bulk nematic phase is oriented uniformly along some direction not specified, implying that $\nabla\theta \rightarrow \mathbf{0}$ as $y \rightarrow \infty$. We anticipate that different nematic textures close to the patterned surface will lead, in general, to distinct nematic far-field orientations, and thus surface transitions will change the nematic anchoring with respect to the substrate reference plane xz . In general different textures have different symmetries, and thus the anchoring transitions are expected to be first-order. Close to the transitions the surface states are locally stable in a thermodynamic sense, and these geometries are ideal candidates for the design of zenithally bistable devices.

The excess free energy F can be written as $F_e + F_a + F_c$, where F_e is the elastic contribution, F_a is the free-energy contribution associated to the anchoring of the nematogen molecules to the substrate and F_c is the contribution associated to the disclination cores. F_e is given by the Frank-Oseen elastic free energy [43, 44]:

$$F_e = \frac{1}{2} \int_{\mathcal{V}} d\mathbf{r} \left[K_1 (\nabla \cdot \mathbf{n})^2 + K_2 (\mathbf{n} \cdot \nabla \times \mathbf{n})^2 + K_3 (\mathbf{n} \times \nabla \times \mathbf{n})^2 + K_{24} \nabla \cdot [(\mathbf{n} \cdot \nabla) \mathbf{n} - \mathbf{n} (\nabla \cdot \mathbf{n})] \right] \quad (1)$$

where \mathcal{V} is the volume occupied by the nematic liquid crystal, K_1 , K_2 and K_3 are the splay, twist and bend bulk elastic constants, respectively, and K_{24} is the saddle-splay elastic constant. Thus, using the parametrization of \mathbf{n} in terms of the field $\theta(x, y)$,

the elastic contribution to the nematic free energy per unit length along the z axis, $f_e = F_e/L_z$, is:

$$f_e = \frac{K_1}{2} \int_{\mathcal{A}} \left(|\nabla\theta|^2 + \left(\frac{K_3 - K_1}{K_1} \right) (\mathbf{n} \cdot \nabla\theta)^2 \right) dx dy \quad (2)$$

where \mathcal{A} is the xy section of the volume occupied by the nematic liquid crystal. Note that the twist and saddle-splay contributions vanish identically. If we further assume that the splay and bend elastic constants are equal, i.e. $K_1 = K_3 = K$, then:

$$f_e = \frac{K}{2} \int_{\mathcal{A}} |\nabla\theta|^2 dx dy \quad (3)$$

The anchoring free-energy contribution F_a is modelled by the Rapini-Papoular approximation [45]

$$F_a = -\frac{W}{2} \int_{\mathcal{S}} ds (\mathbf{n}(\mathbf{s}) \cdot \boldsymbol{\nu}(\mathbf{s}))^2 \quad (4)$$

where the integral is over the substrate surface \mathcal{S} , and $\boldsymbol{\nu}(\mathbf{s})$ is the outwards unit vector normal to the substrate at \mathbf{s} . Thus, the anchoring contribution to the nematic free energy per unit length along the z axis, $f_a = F_a/L_z$, is:

$$f_a = -\frac{W}{2} \int_{\mathcal{L}} ds \cos^2 \psi(s) \quad (5)$$

where \mathcal{L} is the curve $(x, \psi(x), 0)$, parametrized by its natural parameter s , and ψ is the angle between \mathbf{n} and $\boldsymbol{\nu}$, i.e. $\psi = \theta - \alpha$, with $\alpha(x) = \arctan(\psi'(x))$.

In order to obtain the equilibrium nematic texture, we have to minimize the functional $f \equiv f[\theta] = f_e + f_a + f_c$, with f_e and f_a given by Eqs. (3) and (5), respectively. Due to the symmetries of the problem, we have to find the solution only in the xy region R delimited by the dashed line in Fig. 2 and bounded below by one period of the substrate relief. The Euler-Lagrange equation associated to the functional $f[\theta]$ reduces to the Laplace equation in R , $\nabla^2\theta = 0$, subject to the boundary condition on the substrate:

$$\xi_{ext} \boldsymbol{\nu} \cdot \nabla\theta(s) = -\frac{1}{2} \sin 2\psi(s) \equiv -\frac{1}{2} \sin 2(\theta(s) - \alpha(s)) \quad (6)$$

where $\xi_{ext} \equiv K/W$ is the Kléman-de Gennes extrapolation length [16]. In addition, periodic boundary conditions are imposed on the sides $x = -\lambda/2$ and $x = \lambda/2$, and free (Neumann) boundary conditions $\partial\theta/\partial y(y = H) = 0$ at the far field.

Some comments are in order at this point. First, other boundary conditions on the lateral sides are allowed. For example, we can assume that $\theta(x + \lambda, y) = \theta(x, y) + m\pi$, where m is an integer. However, this condition leads to a solution of the Laplace equation which is linear in x far away from the substrate, leading to an infinite interfacial free energy as a result of elastic distortions in the bulk. As we are interested in the anchoring of an undistorted bulk nematic at a patterned substrate, we discard these solutions. On the other hand, we take the limit $H \rightarrow \infty$. Finite values of H are relevant to study nematic textures under confinement.

The continuum model described above is valid as long as all the characteristic relief lengths are much larger than the nematic coherence length ξ_0 , which is of the order of the molecular size. For strong anchoring conditions, $\xi_{ext} \sim \xi_0$ and Eq. (6) can be substituted by the strong anchoring condition $\theta(s) = \alpha(s)$ on the substrate. For weak anchoring, $\xi_{ext} \gg \xi_0$, and in principle this lengthscale is also relevant. In typical liquid crystals $\xi_0 \sim 1$ nm and $\xi_{ext} \sim 0.1 - 10$ μm . However, if we assume that the typical lengthscale which controls the substrate pattern is λ , then strong anchoring conditions on the substrate may be considered also for $\xi_{ext} \gg \xi_0$ if $\lambda \gg \xi_{ext}$. We can justify this result by rescaling the domain by a factor λ [31]: $\mathbf{r}^* = \mathbf{r}/\lambda$ and $\theta^*(\mathbf{r}^*) = \theta(\mathbf{r})$. In order to minimize the free energy functional in this rescaled description, we solve the Laplace equation in the rescaled domain subject to an effective anchoring potential $W^* = \lambda W$ on the substrate, so the rescaled extrapolation length is $\xi_{ext}^* = \xi_{ext}/\lambda \ll 1$ in this limit.

The question about the existence of anchoring transitions in the strong anchoring limit is related to the uniqueness of the solutions of the Laplace equation subject to the boundary conditions described above. A standard analysis of the mathematical problem shows that the Laplace equation is unique for a given integration domain and boundary conditions on the substrate. In fact, the eigenvalues of the Laplacian with the corresponding homogeneous boundary conditions are strictly positive, as inferred from its Rayleigh quotient, and the uniqueness of the solution is guaranteed via Fredholm's alternative. Thus, only one texture is expected under strong anchoring conditions. This result is consistent with previous results in the literature [22, 24, 28], where it is shown that for patterned and/or chemically heterogeneous substrates a unique nematic texture is observed if the extrapolation lengths are much larger than λ . On the other hand, a transition between an almost homogeneous and a distorted texture may be observed if any of the relevant extrapolation lengths is of order of λ [22, 24]. The driving force for this transition is the competition between the elastic and the anchoring contributions to the free energy. This mechanism is not relevant at large λ , since $f_e \sim K$ while $f_a \sim \lambda W$ when λ is large.

However, there is analytical, numerical and experimental evidence that different textures are indeed possible for a given substrate relief, even in the strong anchoring limit [7, 14, 17–19, 30–32, 34, 41]. The apparent contradiction with the previous result may be resolved by noting that some of the textures exhibit topological defects in the nematic, i.e. $\pm 1/2$ disclination lines or, in their absence, the relief has cusps. In the first situation, the presence of a disclination line in the nematic modifies the domain where the Laplace equation is solved, since the solution has a singularity at the defect core. In addition, a branch cut must be added in order to avoid the non-physical (but mathematically sound) jump of θ by $\pm\pi$ when following a loop enclosing the defect core. Thus the domain where the Laplace equation is solved has to be modified by excluding both the defect core and the branch cut, with additional conditions on these new boundaries. Furthermore, the free energy per unit length will have a contribution f_c due to the destruction of orientational order at the core of the disclination line.

On the other hand, when the substrate relief has cusps, the angle θ exhibits a

discontinuity under strong anchoring conditions. This implies that the solution has a disclination-like singularity close to the cusp, with its associated core contribution f_c [32]. The strength of the singularity I , i.e. its effective topological charge, is related geometrically to the opening angle of the cusp $\Delta\phi$ and the jump $\Delta\theta$ of the orientational field θ when crossing the cusp along the surface from right to left as $I = \Delta\theta/\Delta\phi$ [40]. One possibility is that $\Delta\theta_0 = \Delta\phi - \pi$, which leads to $I_0 = 1 - \pi/\Delta\phi$. However, this is not the only option due to the physical equivalence between \mathbf{n} and $-\mathbf{n}$. In particular, it is possible that $\Delta\theta_m = \Delta\theta_0 + m\pi$ for $m \in \mathbb{Z}$, which leads to $I_m = 1 + (m - 1)\pi/\Delta\phi$. In each case, the boundary conditions are mathematically different, although physically equivalent. Thus different textures may occur for the same substrate under strong anchoring conditions.

The elastic energy per unit length along the z axis has contributions associated to the disclination lines and the distortions close to the cusps of the form [40]:

$$\frac{K}{2} \left(\frac{N_D \pi}{2} + \sum_i I_i^2 \Delta\phi_i \right) \ln \left(\frac{\lambda}{\xi_0} \right) \quad (7)$$

where N_D is the total number of disclination lines in the nematic and the index i runs over all the cusps on the substrate. The next-to-leading contribution to the free energy per unit length is expected to be independent of the lengthscale λ . Thus, for large λ we expect only transitions between textures with the same leading-order contribution to the free energy given by Eq. (7). However, we will see that for moderate values of λ other transitions between textures may be observed.

3. Numerical method

Analytical solutions of nematic textures in contact with patterned substrates are not available, in general. There are exceptions, which may be obtained, for example, by using conformal mapping techniques [42]. Otherwise, we have to resort to numerical methods. However, the presence of disclination lines and/or singularities associated to the surface cusps requires special techniques. In this section we will describe the method used to obtain the nematic textures in the presence of disclination lines and/or substrate cusps, which is based on the numerical methods used previously for the sawtooth substrate [32]. First, we will assume that the number and positions of the disclination lines in the nematic are known. In this case, the elastic contribution will be a function of the number of disclination lines and their corresponding positions. Their equilibrium values can be obtained by standard minimization techniques, such as conjugated-gradient methods.

We split the orientation field $\theta(x, y)$ in two terms: a singular contribution θ_s , associated to the disclination lines in the nematic and/or the disclination-like singular contributions due to the surface cusps, and θ_{ns} which we require to be regular everywhere in the integration domain R . If disclination lines are present in the nematic, we modify the integration R to \overline{R} , excluding the defect core and the branch cut, which we will consider perpendicular as shown in Fig. 3. We choose θ_s periodic in x , with period

λ , satisfying the Laplace equation in \overline{R} (R in the absence of disclination lines), which captures the singularities in the orientational field associated to the disclination lines and surface cusps. A possible choice, based in previous studies for the sawtooth substrate, is [31, 32]:

$$\begin{aligned} \theta_s = & \sum_i I_i \left[\arctan \left(\frac{\tanh \frac{q}{2}(y - \psi(x_i))}{\tan \frac{q}{2}(x - x_i)} \right) \right. \\ & \left. - \arctan \left(\frac{1}{\tan \frac{q}{2}(x - x_i)} \right) \right] \\ & + \sum_j I_j \left[\arctan \left(\frac{\tanh \frac{q}{2}(y - y_j)}{\tan \frac{q}{2}(x - x_j)} \right) \right. \\ & \left. + \arctan \left(\frac{1}{\tan \frac{q}{2}(x - x_j)} \right) \right] \end{aligned} \quad (8)$$

where $q = 2\pi/\lambda$, the first sum runs over the surface cusps at $(x_i, \psi(x_i))$, while the second one is over the disclination lines at positions (x_j, y_j) in the nematic phase. Note that the contribution associated to the surface cusps vanishes as $y \rightarrow \infty$. By contrast, the nematic disclination term exhibits a piecewise linear behaviour as $y \rightarrow \infty$ and its elastic contribution to the interfacial free energy diverges unless the total topological charge associated to the nematic disclination lines vanishes. Therefore, we restrict our study to situations where the number of $+1/2$ -disclination lines in the nematic phase is the same as the number of $-1/2$ -disclination lines to ensure that the far-field director field is undistorted.

For the non-singular part θ_{ns} , we have to solve the Laplace equation subject to periodic boundary conditions on the sides $x = \pm\lambda/2$ and free boundary conditions as $y \rightarrow \infty$. Finally, θ_{ns} satisfies Dirichlet boundary conditions $\theta_{ns}(s) = \alpha(s) - \theta_s(s)$ at the substrate. As mentioned above, the regularity of θ_{ns} in the region R implies that standard numerical techniques can be used. We use the boundary element method to obtain θ_{ns} in the constant element approximation [46, 47]. In Ref. [32] we used a boundary-element method where the whole boundary of R is discretized. In this paper we use a different boundary-element method that requires only the discretization of the substrate relief. A detailed description of this technique can be found in Appendix A. For this purpose, a polygonal approximation to the substrate relief is considered, where each segment length is small with respect to λ (the only lengthscale relevant for this problem). Thus, for the sawtooth and sinusoidal substrates, the substrate is divided into 720 segments with the same x -axis projection length. On the other hand, for the crenellated substrate each side of the substrate is divided into 120 segments of the same length. We checked that our numerical results are, within numerical accuracy, almost identical when finer discretizations are considered.

Once the orientational field is obtained, we need to evaluate the corresponding interfacial free energy. The elastic contribution to the free energy per z -unit length

and x -period f_e can be obtained from Eq. (3) as:

$$f_e = \frac{K}{2} \int_{\mathcal{A}} |\nabla\theta|^2 d\mathbf{r} = \frac{K}{2} \oint \theta(\boldsymbol{\nu} \cdot \nabla\theta) ds \quad (9)$$

Technical details on how to evaluate this contribution from the singular and non-singular parts of the orientational field are described in Appendix B.

The final ingredients are the core contributions f_c arising from the disclination lines and the effective disclination-like singularities of the nematic textures. These terms are not described by the macroscopic elastic theory, and we have to resort to a more microscopic description to evaluate them. We will evaluate them using the mesoscopic Landau-de Gennes framework $F_{LdG} = \int_{\mathcal{V}} d\mathbf{r} (\mathcal{F}_b(\mathbf{Q}) + \mathcal{F}_e(\partial\mathbf{Q})) + \int_{\mathcal{S}} \mathcal{F}_s(\mathbf{Q})$, where the bulk and elastic free energy densities are, respectively,

$$\mathcal{F}_b = a_o (T - T^*) \text{Tr} \mathbf{Q}^2 - b \text{Tr} \mathbf{Q}^3 + c (\text{Tr} \mathbf{Q}^2)^2 \quad (10)$$

$$\mathcal{F}_e = \frac{L_1}{2} \partial_\gamma Q_{\alpha\beta} \partial_\gamma Q_{\beta\alpha} + \frac{L_2}{2} \partial_\gamma Q_{\alpha\gamma} \partial_\delta Q_{\delta\alpha}. \quad (11)$$

The bulk term \mathcal{F}_b determines the bulk nematic order parameter: $S = 0$ (isotropic phase) if $\tau = 24a_o(T - T^*)c/b^2 > 1$, and $S = (b/8c) \left(1 + \sqrt{1 - 8\tau/9}\right)$ (nematic phase) if $\tau < 1$. The elastic term \mathcal{F}_e penalizes distortions of the orientational field, with two elastic constants L_1 and L_2 related to the Frank-Oseen elastic constants: $K_1 = K_3 = 9S^2 L_1 (2 + L_2/L_1)/4$ and $K_2 = 9S^2 L_1/2$. In addition, we consider the surface free energy density used in Refs. [31, 32, 36–38, 40]:

$$\mathcal{F}_s = -w \text{Tr} \mathbf{Q} \cdot \mathbf{Q}_s \quad (12)$$

where w is a parameter related to the anchoring strength [32] and \mathbf{Q}_s is the reference tensor order parameter on the substrate with Cartesian components $(Q_s)_{ij} = (3\nu_i\nu_j - \delta_{ij})/2$, and ν_i the Cartesian components of the unit vector normal to the substrate $\boldsymbol{\nu}$. We obtain the core contributions by using an adaptive-meshing finite-element method combined with a conjugate-gradient minimization algorithm, following the procedure described in Ref. [32]. Note that, as the typical size of the cores is ξ_0 , the cores associated with the disclination lines in the nematic are independent from the substrate. This is not the case at the cusps where we assume that two locally planar surfaces meet. The core contribution of the cusp singularities depends, in general, on the anchoring strength. In what follows, we take the nematic to be at nematic-isotropic coexistence (i.e. $\tau = 1$).

4. Results

In this Section we will describe the results for different substrate reliefs. In particular, we will revisit the sawtooth case, and we will present results for the crenellated and the sinusoidal substrates.

4.1. The sawtooth substrate

The sawtooth substrate has been studied for a number of years [28, 31, 32]. We revisit some of the results reported previously. We consider a symmetric sawtooth,

characterized by a tilt angle α and a side length L , as shown in Fig. 4(a), so that $\lambda = 2L \cos \alpha$. No bulk disclinations are expected in the nematic texture, at least at distances of order L from the substrate. It is found that there are two nematic textures that are locally stable: the N^\perp texture, where the nematic field is oriented along the y axis away from the substrate, in the far field, and the N^\parallel texture, where the nematic field is oriented along the x axis in the far field, as shown in Fig. 5. These textures are characterized by different effective topological charges I^t and I^b associated to the top and bottom cusps, respectively. In the N^\perp texture, $I^t = I_0^t \equiv \alpha/(\pi/2 + \alpha)$ and $I^b = I_0^b \equiv -\alpha/(\pi/2 - \alpha)$, while in the N^\parallel texture, $I^t = I_{+1}^t \equiv -(\pi/2 - \alpha)/(\pi/2 + \alpha)$ and $I^b = I_{+1}^b \equiv 1$. The elastic contribution to the interfacial free energy f_e of the nematic (per z -unit length and x -period) at this substrate was obtained analytically [32]:

$$\begin{aligned}
 f_e = \mathcal{K}_m(\alpha) & \left[-\ln \frac{q\xi_0 \cos \alpha}{\pi} - \left(\frac{1}{2} - \frac{\alpha}{\pi} \right) \ln \left(\frac{\frac{\pi}{2} + \alpha}{\frac{\pi}{2} - \alpha} \right) \right. \\
 & \left. - \ln \left(\Gamma \left[\frac{3}{2} - \frac{\alpha}{\pi} \right] \Gamma \left[\frac{1}{2} + \frac{\alpha}{\pi} \right] \right) \right]
 \end{aligned} \quad (13)$$

where $m = 0$ for the N^\perp texture and $m = +1$ for the N^\parallel texture. The meaning of these numbers will be discussed below. The effective elastic constants \mathcal{K}_0 and \mathcal{K}_{+1} are

$$\mathcal{K}_0(\alpha) = \frac{K\pi\alpha^2}{\left(\frac{\pi}{2}\right)^2 - \alpha^2} \quad ; \quad \mathcal{K}_{+1}(\alpha) = K\pi \frac{\frac{\pi}{2} - \alpha}{\frac{\pi}{2} + \alpha} \quad (14)$$

Numerical results are in excellent agreement with the analytical result (see Ref. [32] for a more detailed discussion). As $\mathcal{K}_0(\pi/4) = \mathcal{K}_{+1}(\pi/4)$, there is an anchoring transition from homeotropic to planar anchoring at $\alpha = \pi/4$. However, the value of α at the transition may be altered in two ways. First, the core contributions f_c associated to the effective disclination-like singularities may be different for the N^\perp and N^\parallel textures. These core contributions will shift the transition (from $\alpha = \pi/4$) by a small amount, since $f_c \ll f_e \sim K \ln \lambda/\xi_0$ for large λ . Alternatively, for $\alpha = \pi/4$ this contribution drives the transition between the N^\perp and N^\parallel when varying the value of the anchoring strength w .

The elastic constants anisotropy can also cause a shift in the anchoring transition. In the previous discussion we assumed that the splay and bend elastic constants are equal, in line with the observation that $K_3/K_1 - 1$ is very small for liquid crystals like 5CB, close to the nematic-isotropic phase transition. In order to estimate the effect of the elastic anisotropy on the anchoring transition, a perturbation theory around the one-elastic constant model was developed [28]. The first order correction in $K_3/K_1 - 1$ is obtained using Eq. (2) [28]:

$$\frac{K_3 - K_1}{2} \int_{\mathcal{A}} dx dy (\mathbf{n}_0 \cdot \nabla \theta_0)^2 \quad (15)$$

where θ_0 is the nematic orientation field for $K_1 = K_3$ and $\mathbf{n}_0 = (-\sin \theta_0, \cos \theta_0, 0)$. The main contribution arises from the neighbourhood of the cusps, which leads to an additional term proportional to $(K_3 - K_1) \ln \lambda/\xi_0$. We refrain from giving explicit expressions for this leading-order correction, which implies that the anchoring transition

shifts to $\alpha > \pi/4$ if $K_3 > K_1$, and below $\pi/4$ otherwise. Physically this is due to the fact that the elastic distortions in the N^\perp texture are mainly splay, while bend dominates in the N^\parallel texture (see Fig. 5).

Finally, N^\perp and N^\parallel are not the only textures that are possible at a sawtooth substrate. As mentioned in Section 2, the effective topological charges associated with the disclination-like singularities arising from the substrate cusps may be expressed as $I_0 + m\pi$, where I_0 is one possible value of the topological charge and m is an integer. Therefore, there is an infinite number of (pairs) of topological charges I^b and I^t , since $I_m^b = -\alpha/(\pi/2 - \alpha) + m\pi/(\pi - 2\alpha)$ and $I_{-m}^t = \alpha/(\pi/2 + \alpha) + m'\pi/(\pi - 2\alpha)$ and the periodicity requirement on θ imposes $m' = -m$. The boundary conditions on θ are then $\theta = -\alpha$ on the left-to-right uphill segments, and $\theta = -\alpha + m\pi$ on the downhill segments. The far-field value α_∞ is the average of these, $\alpha_\infty = m\pi/2$, which is the value of θ along the vertical lines emerging from the substrate cusps. Note that if $m = 0$ and $m = +1$ we obtain the N^\perp and the N^\parallel textures, respectively, in line with the notation used in Eqs. (13) and (14). The free energy of these nematic textures may be solved using the Schwarz-Christoffel conformal mapping used for the N^\perp and N^\parallel cases, leading to an elastic contribution to the interfacial free energy given by Eq. (13), with \mathcal{K}_m defined as:

$$\begin{aligned} \mathcal{K}_m(\alpha) &= \frac{K}{2} \left[(I_m^b)^2 (\pi - 2\alpha) + (I_{-m}^t)^2 (\pi + 2\alpha) \right] \\ &= \frac{K\pi}{\left(\frac{\pi}{2}\right)^2 - \alpha^2} \left(m\frac{\pi}{2} - \alpha \right)^2 = \mathcal{K}_0(\alpha) \left(\frac{m\pi}{2\alpha} - 1 \right)^2 \end{aligned} \quad (16)$$

Fig. 6 illustrates \mathcal{K}_m as a function of α . The lowest curves, with $m = 0$ and $m = +1$, correspond to the N^\perp and N^\parallel textures, respectively. The other curves describe higher elastic energy states, and may be discarded at equilibrium. A similar behaviour was found for isolated wedges [42].

4.2. The crenellated substrate

We proceed with the crenellated substrate, characterized by infinite blocks of width and height l_1 and h , respectively at a distance l_2 , as shown in Fig. 4(b). The substrate relief period is $\lambda = l_1 + l_2$. As in the sawtooth, the presence of cusps in the substrate relief leads to the appearance of disclination-like singularities in the orientational field nearby. By geometric considerations, the topological charges associated with the upper cusps (i.e. with opening angles $3\pi/2$), I_1^t and I_2^t , will be either $+1/3$ or $-1/3$, and the charges associated with the lower cusps (i.e. with opening angles $\pi/2$), I_1^b and I_2^b , will be either $+1$ or -1 . As in the sawtooth, not every combination is possible due to the periodicity constraint. In order to ensure periodicity there must be two positive topological charges (with the other two negative). Other values of the topological charges are possible, but as in the sawtooth case, they lead to much higher elastic free energies, which are irrelevant at equilibrium. Thus, we find 4 independent nematic textures: N_1^\perp , where $I_1^t = I_2^t = -1/3$ and $I_1^b = I_2^b = +1$; N_2^\perp , with $I_1^t = I_2^t = +1/3$ and $I_1^b = I_2^b = -1$; N_1^\parallel with $I_1^t = -1/3$, $I_1^b = +1$, $I_2^t = +1/3$ and $I_2^b = -1$, and finally N_2^\parallel with $I_1^t = -1/3$, $I_1^b = -1$,

$I_2^t = +1/3$ and $I_2^b = +1$. Nematic textures obtained by the numerical minimization described in the previous section are shown in Fig. 7. Note that both N_1^\perp and N_2^\perp are symmetric with respect to a mirror inversion, while N_1^o and N_2^o are asymmetric. Thus, for the latter there are two other equivalent textures related by mirror symmetry. With respect to the bulk nematic anchoring, the symmetric textures are homeotropic, i.e. the nematic director is oriented along the y axis far away from the substrate. The asymmetric textures, however, exhibit oblique nematic anchoring. The far-field tilt angle α_∞ of the N_1^o texture depends on h/l_2 and l_1/l_2 . For a given value of l_1/l_2 it increases monotonically with h/l_2 from zero and reaches a plateau at large h above $h/l_2 \gtrsim 1$. The asymptotic values of α_∞ at large h/l_2 decrease as l_1/l_2 increases, being almost proportional to $l_1/(l_1 + l_2)$ at large l_1 . Thus, narrow blocks lead to values of $\alpha_\infty \approx \pi/2$, while narrow channels lead to nearly homeotropic anchoring. Our numerical data also indicates that α_∞ satisfies approximately $\alpha(h/l_2; l_1/l_2) \approx \alpha_\infty(\infty; l_1/l_2)\chi(h/l_2)$ (see the inset of Fig. 8). The existence of a plateau in α_∞ at large h can be explained by noting that the nematic director in the region between the blocks at height $y \lesssim h - l_2$ (provided that $h \gg l_2$) is almost the same as that in a rectangular well [42]. This solution becomes almost parallel to the x axis for $l_2 \lesssim y - l_2$. In this case, the dependence on h is irrelevant at $h \gtrsim l_2$, leading to the same orientation field above the substrate blocks. On the other hand, the value of $\alpha_\infty(\infty; l_1/l_2)$ decreases as l_1/l_2 increases because the final anchoring results from a competition between the homeotropic anchoring favoured by the top of the blocks, and the planar anchoring favoured by the rectangular wells.

The equilibrium texture for each substrate is that which minimizes the free energy. First, we note that the leading-order contributions due to the cusp singularities Eq. (7) are equal to $2\pi K/3$ for all the textures. Therefore, this term will be irrelevant to identify which texture is the equilibrium one for a given substrate relief, so we need to analyse the next-to-leading order contributions. As shown in Ref. [32] for the sawtooth substrate, we have to consider a term of elastic origin, in addition to the contribution of the cores corresponding to the disclination-like singularities close to the cusps, to fully account for the next-to-leading contribution to the interfacial free energy per z -unit length and x -period. First we analyse the elastic contribution, which depends on l_1 , l_2 and h through two independent ratios h/l_2 and l_1/l_2 , or equivalently, on the roughness $r = 1 + 2h/(l_1 + l_2)$ and l_1/l_2 [40]. The results of our calculations show that the N_2^o texture has always a higher elastic free energy than the other textures, so it can be discarded from the discussion. Fig. 7 illustrates this point showing that the distortions of the nematic director field are more pronounced in the N_2^o texture than in the other textures. Another interesting observation is that both symmetric textures have the same elastic free energy. This is shown analytically in the Appendix C, where the exact elastic contribution to the free energy of the symmetric textures is calculated. The numerical results are in excellent agreement with the analytical results, as can be seen in Fig. 9(a), although some deviations are visible for very shallow and/or narrow crenels. This observation provides a stringent test of the numerical accuracy. Purely elastic arguments predict that the N_1^o state is the lowest free-energy texture at all crenellated substrates,

as shown in Fig. 9(a). However, the free-energy of the symmetric and asymmetric textures approach each other at small values of the roughness and thus, the cusp singularity cores contribution to the free energy may stabilize the symmetric textures with respect to the tilted one. In Fig. 9(b) we plot the core contributions associated to the different cusps and topological charges, as well as the total contribution for each nematic texture. Note that the total core contribution for a surface state corresponding to a nematic texture is just the sum of the contributions associated to each isolated cusp, regardless the substrate geometry. This contribution breaks the free-energy degeneracy of the symmetric textures, favouring the N_2^\perp texture at small and large values of w , and the N_1^\perp texture otherwise. The core contribution associated to the N_1^o texture is always higher than that corresponding to the least free-energy symmetric texture, since the tilted texture core contribution is the average of the values of the symmetric textures. So, if the core contribution of the tilted configuration exceeds the elastic free-energy difference between the symmetric and the N_1^o textures, the corresponding symmetric state may be stabilized. Fig. 10 depicts the global phase diagram of the crenellated substrate. At large substrate roughness, the tilted nematic texture is the most stable phase. By decreasing the roughness, a transition to a symmetric texture may be observed. These findings are in agreement with previous experimental [14] and Landau-de Gennes numerical [40] results. At low and high values of the anchoring parameter w , the symmetric state is N_2^\perp , while for intermediate values of w it is N_1^\perp . Furthermore, reentrant behaviour is found at intermediate values of w . The phase boundaries move to higher values of h/l_2 as l_1/l_2 , but they saturate at $h/l_2 \gtrsim 1$.

Finally, we comment on the effect of the anisotropy of the elastic constants. As discussed for the sawtooth substrate, the main effect of the anisotropy is to shift the leading-order elastic free-energy contribution. Therefore, if λ/ξ_0 is large, then the N_1^\perp (N_2^\perp) texture is favoured when $K_3 > K_1$ ($K_3 < K_1$), respectively. By comparison with the sawtooth substrate, the leading contributions are again identical for the three nematic textures at crenellated substrate where blocks have tilted lateral sides. However, if $|K_3/K_1 - 1| \ln(\lambda/\xi_0)$ is of order of the next-to-leading contribution when $K_1 = K_3$, then this is another contribution to take into account when evaluating the phase diagram.

4.3. The sinusoidal substrate

We now turn to a sinusoidal substrate of period λ and amplitude A . This has also been studied previously [15, 21, 28, 33, 38]. As the substrate relief does not have cusps, a state without defects is expected to be the least free-energy state. This state exhibits homeotropic anchoring, i.e. the far-field nematic director is oriented along the y axis, for all qA (see Fig. 11(a)). We denote this texture by N^\perp . As qA increases, the substrate roughness increases, and the orientational field exhibits large distortions to follow the anchoring at the substrate. Numerical results show that, under these circumstances, the elastic distortions are lowered by reorienting the nematic director field, in the groove, along the x axis (see Fig. 11(b)), and thus the texture exhibits planar anchoring,

denoted by N^{\parallel} . This texture involves the nucleation of two disclination lines with opposite topological charges, located by symmetry above the top and bottom of the substrate relief, at a distance plotted in Fig. 12. This distance is proportional to λ , and in the limit of large λ , the disclination lines are not affected by the substrate. The distance decreases as the substrate roughness increases until it stabilizes for $qA > 2$. Thus, in an effective way, the disclinations lines are bound to the surface relief (on the λ scale), driving the orientational field almost horizontal everywhere. At large λ , the interfacial free energy of the N^{\perp} texture depends on A and λ through the factor qA which determines the substrate roughness. On the other hand, from Eq. (7) the interfacial free energy of the N^{\parallel} texture has a leading contribution $(K\pi/2) \ln \lambda/\xi_0$, and the next-to-leading term has the same qA dependence as above. Note that, in this case, we have to add the core contributions associated to the $\pm 1/2$ disclinations lines, with constant values $f_c(I = +1/2)/K = 0.63 \pm 0.01$ and $f_c(I = -1/2)/K = -0.14 \pm 0.01$. Thus, at large λ only the N^{\perp} texture is expected for any substrate roughness. However, the weak dependence of the interfacial free energy of the N^{\parallel} texture on λ implies that, for moderate values of λ , an anchoring transition between the N^{\perp} and N^{\parallel} textures may be observed. Fig. 13 shows the interfacial free energy of the N^{\perp} and N^{\parallel} textures as a function of qA , for different values of λ . While the N^{\perp} branch depends only on qA and is an increasing function of this parameter, the N^{\parallel} branches are decreasing functions of qA , and for different values of λ are shifted by the $\ln \lambda$ term.

Fig. 14 shows the $qA - \lambda$ anchoring phase diagram. The homeotropic anchoring state N^{\perp} is favoured at low qA , while at large substrate roughness planar anchoring is observed, i.e. the N^{\parallel} has the lowest free energy. We note that the value of λ at the transition increases almost exponentially with qA .

Finally, as in the previous cases we can include the effect of the anisotropy of the elastic constants perturbatively. If we assume that the elastic distortions are on the xy plane, the conclusion is that the anchoring transition, which corresponds to moderate values of λ , may be shifted by this contribution, although qualitatively it will be very similar. However, if the twist elastic constant is smaller than K , there is experimental [11] and numerical [48] evidence of a twist instability which breaks the azimuthal symmetry: the disclination line is no longer parallel to the z axis, but exhibits a zig-zag structure which decreases the splay and bending distortions. This cannot happen in the sawtooth and crenellated substrates, since the disclination-like singularities are located at the surface cusps.

5. Conclusions

In this paper we report the results of a numerical investigation of the equilibrium nematic textures at patterned substrates under strong anchoring conditions. We characterize the surface phase diagram of nematic textures which differ in the tilt angle of the far-field nematic director with respect to the substrate reference plane. First-order phase transitions between these surface states, i.e. anchoring transitions, are observed

when the geometric features of the surface relief are varied, although there are other control parameters (such as the anchoring surface strength) which may play a role in the location of the phase boundaries. Our findings, which generalize previous work by the authors [32], differ from previous results for weak anchoring conditions, where these anchoring transitions are driven by the competition between the elastic deformations in the nematic orientational field and the surface anchoring energy. By contrast, in the strong-anchoring regime, these transitions are a direct outcome of the interplay between the elastic deformations and the formation of disclinations and disclination-like singularities near surface cusps. In addition, a small elastic anisotropy can play a similar role to that of these topological defects. To illustrate our study, we consider three substrate reliefs: the sawtooth substrate, the crenellated substrate and the sinusoidal substrate. For the sawtooth and sinusoidal substrates, we observed a homeotropic to planar anchoring transition as the substrate roughness is increased. On the other hand, the crenellated substrate exhibits a more complex anchoring phase diagram, with a homeotropic to oblique anchoring transition, which depends not only on the substrate roughness but also on the surface anchoring strength. The latter results from the dependence of the core contribution of the cusp singularities on the anchoring strength.

Some final remarks are in order. Although we used the Landau-de Gennes model to obtain the defect core contributions to the free energy, any other model could be considered. This may change the results quantitatively, when this contribution is relevant as for the crenellated substrates, but not qualitatively. Secondly, our procedure can be easily modified to consider the presence of nematic-isotropic interfaces. This allows the study of wetting, filling and related interfacial phenomena for nematic liquid crystals. This is ongoing work, and will be published elsewhere. Finally, we restricted the nematic orientational distortions to the plane perpendicular to the longitudinal axis of the surface. The generalization to full three-dimensional systems to consider situations where twist [11, 49] or saddle-splay [50, 51] distortions play a role is a formidable task which is currently beyond the scope of our work.

Acknowledgments

We acknowledge financial support from the Portuguese Foundation for Science and Technology under Contracts Nos. EXCL/FIS-NAN/0083/2012 and UID/FIS/00618/2013 (NMS and MMTG). O.A.R.-G. and J.M.R.-E. also acknowledge partial financial support from the Spanish Ministerio de Economía y Competitividad through grant no. FIS2012-32455, and Junta de Andalucía through grant no. P09-FQM-4938, all co-funded by the EU FEDER.

Appendix A. Evaluation of θ_{ns} using the boundary element method

The field θ_{ns} , as a solution of the Laplace equation on R , has the boundary integral representation:

$$\begin{aligned} \theta_{ns}(\mathbf{r}) = \oint_{\partial R} ds \left([\boldsymbol{\nu}(\mathbf{s}) \cdot \nabla_{\mathbf{s}} \theta_{ns}(\mathbf{s})] G(\mathbf{s}, \mathbf{r}) \right. \\ \left. - \theta_{ns}(\mathbf{s}) [\boldsymbol{\nu}(\mathbf{s}) \cdot \nabla_{\mathbf{s}} G(\mathbf{s}, \mathbf{r})] \right) \end{aligned} \quad (\text{A.1})$$

where the contour integral over the boundary ∂R of R is counter-clockwise, $\boldsymbol{\nu}(\mathbf{s})$ is the outwards normal to the boundary at \mathbf{s} and $G(\mathbf{r}, \mathbf{r}_0)$ is the fundamental solution of the Laplace equation in the infinite strip $-\lambda/2 \leq x \leq \lambda/2$, $-\infty < y < \infty$ with periodic boundary conditions on x :

$$G(\mathbf{r}, \mathbf{r}_0) = -\frac{1}{4\pi} \ln (\cosh q(y - y_0) - \cos q(x - x_0)) \quad (\text{A.2})$$

where $\mathbf{r} = (x, y)$ and $\mathbf{r}_0 = (x_0, y_0)$. Note that this solution can be obtained as the composition of the fundamental solution on the free plane $-\ln|\mathbf{r}|/(2\pi)$ and the conformal mapping $\zeta = \sin q(z - z_0)/2$ which maps the strip onto the full complex plane. As both θ_{ns} and G are periodic on x with period λ , the contributions to the integral (A.1) from the lateral sides $x = \pm\lambda/2$ cancel each other. On the other hand, $G(\mathbf{r}, \mathbf{r}_0) \approx -|y - y_0|/(2\lambda) + \ln 2/(4\pi)$ at large y . As we impose $\theta_{ns} \rightarrow \theta_{ns}^\infty$ and $\partial\theta_{ns}/\partial y \rightarrow 0$ as $y \rightarrow \infty$, the contribution to the integral (A.1) from the top boundary $y = H \rightarrow \infty$ is equal to $\theta_{ns}^\infty/2$. Therefore, Eq. (A.1) can be rewritten as:

$$\begin{aligned} \theta_{ns}(\mathbf{r}) = \frac{\theta_{ns}^\infty}{2} + \int_{\mathcal{L}} ds \left([\boldsymbol{\nu}(\mathbf{s}) \cdot \nabla_{\mathbf{s}} \theta_{ns}(\mathbf{s})] G(\mathbf{s}, \mathbf{r}) \right. \\ \left. - \theta_{ns}(\mathbf{s}) [\boldsymbol{\nu}(\mathbf{s}) \cdot \nabla_{\mathbf{s}} G(\mathbf{s}, \mathbf{r})] \right) \end{aligned} \quad (\text{A.3})$$

We impose Dirichlet boundary conditions on the substrate relief, so the last term on the right-hand side of Eq. (A.1) is known. The unknowns are the normal derivatives of θ_{ns} on the substrate and the far-field value θ_{ns}^∞ . The former is obtained by solving the integral equation [46, 47]:

$$\begin{aligned} \int_{\mathcal{L}} ds [\boldsymbol{\nu}(\mathbf{s}) \cdot \nabla_{\mathbf{s}} \theta_{ns}(\mathbf{s})] G(\mathbf{s}, \mathbf{s}_0) = \frac{\theta_{ns}(\mathbf{s}_0) - \theta_{ns}^\infty}{2} \\ + \int_{\mathcal{L}} ds \theta_{ns}(\mathbf{s}) [\boldsymbol{\nu}(\mathbf{s}) \cdot \nabla_{\mathbf{s}} G(\mathbf{s}, \mathbf{s}_0)] \end{aligned} \quad (\text{A.4})$$

where $\mathbf{s}_0 \in \mathcal{L}$. On the other hand, for large y , $\theta_{ns}(\mathbf{r}) \approx \theta_{ns}^\infty$ and Eq. (A.3) reduces to

$$\begin{aligned} \theta_{ns}^\infty = \int_{\mathcal{L}} ds [\boldsymbol{\nu}(\mathbf{s}) \cdot \nabla_{\mathbf{s}} \theta_{ns}(\mathbf{s})] \left(\frac{s_y - y}{\lambda} + \frac{\ln 2}{2\pi} \right) \\ - \frac{1}{\lambda} \int_{\mathcal{L}} ds \theta_{ns}(\mathbf{s}) \nu_y(\mathbf{s}) \\ = \frac{1}{\lambda} \int_{\mathcal{L}} ds (s_y [\boldsymbol{\nu}(\mathbf{s}) \cdot \nabla_{\mathbf{s}} \theta_{ns}(\mathbf{s})] - \theta_{ns}(\mathbf{s}) \nu_y(\mathbf{s})) \end{aligned} \quad (\text{A.5})$$

where s_y and ν_y are the y -components of \mathbf{s} and $\boldsymbol{\nu}$, respectively, and the second equality results from the fact that

$$\begin{aligned} 0 &= \int_{\mathcal{A}} d\mathbf{r} \nabla^2 \theta_{ns} = \oint d\mathbf{s} [\boldsymbol{\nu}(\mathbf{s}) \cdot \nabla_{\mathbf{s}} \theta_{ns}(\mathbf{s})] \\ &= \int_{\mathcal{L}} d\mathbf{s} [\boldsymbol{\nu}(\mathbf{s}) \cdot \nabla_{\mathbf{s}} \theta_{ns}(\mathbf{s})] \end{aligned} \quad (\text{A.6})$$

Finally, substituting Eq. (A.5) in Eq. (A.4), we obtain:

$$\begin{aligned} \int_{\mathcal{L}} d\mathbf{s} [\boldsymbol{\nu}(\mathbf{s}) \cdot \nabla_{\mathbf{s}} \theta_{ns}(\mathbf{s})] \left(G(\mathbf{s}, \mathbf{s}_0) + \frac{s_y}{2\lambda} \right) &= \frac{\theta_{ns}(\mathbf{s}_0)}{2} \\ + \int_{\mathcal{L}} d\mathbf{s} \theta_{ns}(\mathbf{s}) \left[\boldsymbol{\nu}(\mathbf{s}) \cdot \nabla_{\mathbf{s}} G(\mathbf{s}, \mathbf{s}_0) + \frac{\nu_y}{2\lambda} \right] \end{aligned} \quad (\text{A.7})$$

In order to solve Eq. (A.7), we discretize the boundary as a set of straight segments (the boundary elements). It is important to ensure that the substrate cusps correspond to extremes of these segments. We use the constant boundary element approach [47], and thus assume that both θ_{ns} and its normal derivative are constant along each boundary element. Introducing this approximation into Eq. (A.7), we obtain a set of linear algebraic equations for the normal derivatives. Once this is solved, the far-field orientation θ_{ns}^∞ is obtained from Eq. (A.5).

Appendix B. Evaluation of the elastic contribution to the interfacial free energy f_e

The value of f_e can be expressed as a contour integral, Eq. (9). Using the periodicity of θ on the boundaries $x = \pm\lambda/2$ and the free boundary at $y \rightarrow \infty$, the contour integral on the right-hand side of Eq. (9) is written as:

$$\frac{K}{2} \int_{\mathcal{L}} \theta(\boldsymbol{\nu} \cdot \nabla \theta) d\mathbf{s} + \sum_{j=1}^{N_D} 2\pi I_j \int_{y_j}^{\infty} dy \left(\frac{\partial \theta}{\partial x} \right)_{x=x_j} \quad (\text{B.1})$$

where the first integral is on the surface relief, and the other terms are on the branch cuts \mathcal{B}_j starting at the disclination j position (x_j, y_j) with topological charge I_j . Finally, we use $\theta = \theta_s + \theta_{ns}$ in the derivatives, and the elastic contribution becomes:

$$\begin{aligned} \frac{K}{2} \int_{\mathcal{L}} \theta(\boldsymbol{\nu} \cdot \nabla \theta_s) d\mathbf{s} + \sum_{j=1}^{N_D} 2\pi I_j \int_{y_j}^{\infty} dy \left(\frac{\partial \theta_s}{\partial x} \right)_{x=x_j} \\ + \frac{K}{2} \int_{\mathcal{L}} \theta(\boldsymbol{\nu} \cdot \nabla \theta_{ns}) d\mathbf{s} + \sum_{j=1}^{N_D} 2\pi I_j \int_{y_j}^{\infty} dy \left(\frac{\partial \theta_{ns}}{\partial x} \right)_{x=x_j} \end{aligned} \quad (\text{B.2})$$

The first two terms exhibit singularities associated to the cusps (first integral) and disclination cores (second term) which must be handled carefully by deforming the contour with arcs of circle of radii ξ_0 to avoid them. In fact, these singularities lead to the contribution Eq. (7) mentioned above. The first integral can be obtained using the substrate relief discretization considered to obtain θ_{ns} . Thus, if we consider the

boundary as the union of \mathcal{L}_k segments ($k = 1, \dots, N_e$, ordered counterclockwise), the first integral may be approximated as:

$$\frac{K}{2} \int_{\mathcal{L}} \theta(\boldsymbol{\nu} \cdot \nabla \theta_s) ds \approx \sum_{k=1}^{N_e} \frac{K}{2} \theta_k \boldsymbol{\nu}_k \cdot \int_{\mathcal{L}_k} \nabla \theta_s ds \quad (\text{B.3})$$

where θ_k and $\boldsymbol{\nu}_k$ are the segment midpoint and the outwards unit normal to that segment \mathcal{L}_k , respectively. Substitution of the expression for θ_s Eq. (8) into Eq. (B.3) leads after some algebra to:

$$\begin{aligned} & \frac{K}{2} \sum_i I_i^2 \Delta \phi_i \left(\ln \left(\frac{\lambda}{\xi_0} \right) - \ln \sqrt{2\pi} + \frac{q y_i}{2} \right) \\ & + \frac{K}{2} \sum_i \sum'_k I_i \Delta \theta_k \\ & \times \left(\frac{1}{2} \ln (\cosh q(y_k - y_i) - \cos q(x_k - x_i)) - \frac{q}{2} y_k \right) \\ & + \frac{K}{2} \sum_j \sum_k I_j \Delta \theta_k \\ & \times \left(\frac{1}{2} \ln (\cosh q(y_k - y_j) - \cos q(x_k - x_j)) + \frac{q}{2} y_k \right) \end{aligned} \quad (\text{B.4})$$

The first term in Eq. (B.4) corresponds to the contribution associated to the surface cusps. In the second term, the sum on i is over the number of cusps, while the sum on k is over the boundary elements. In this expression, (x_i, y_i) is the position of the cusp, I_i is the effective topological charge of the cusp singularity, (x_k, y_k) are the coordinates of the left extreme of the segment \mathcal{L}_k and $\Delta \theta_k = \theta_k - \theta_{k-1}$ with $\theta_0 \equiv \theta_{N_e}$. The prime denotes that we exclude from the sum the nodes that correspond to surface cusps. Finally, in the last term the sum on j is over the disclination lines at positions (x_j, y_j) with topological charges I_j , while the other terms have the same meaning as before.

The second term in Eq. (B.2) can be obtained analytically as:

$$\begin{aligned} & \frac{K\pi N_D}{4} \left(\ln \left(\frac{\lambda}{\xi_0} \right) - \ln \pi \right) + \frac{K\pi}{4} \sum_j q y_j \\ & + \frac{K}{2} \sum_i \sum_j 2\pi I_i I_j \left(\frac{q}{2} (y_i - y_j) + \frac{\ln 2}{2} \right. \\ & \left. + \frac{1}{2} \ln (\cosh q(y_i - y_j) - \cos q(x_i - x_j)) \right) \\ & + \frac{K}{2} \sum_j \sum'_{j'} 2\pi I_j I_{j'} \left(\frac{q}{2} (y_{j'} + y_j) + \frac{\ln 2}{2} \right. \\ & \left. + \frac{1}{2} \ln (\cosh q(y_{j'} - y_j) - \cos q(x_{j'} - x_j)) \right) \end{aligned} \quad (\text{B.5})$$

where the sum on i is over the surface cusps, the sums on j and j' are over the disclination lines, and in the last term the prime denotes that we exclude from the sum terms with $j = j'$.

The last two contributions to Eq. (B.2) associated with θ_{ns} can be obtained in a similar way. The third term yields

$$\frac{K}{2} \int_{\mathcal{L}} \theta(\boldsymbol{\nu} \cdot \nabla \theta_{ns}) ds \approx \sum_{k=1}^{N_e} \frac{K}{2} \ell_k \theta_k (\boldsymbol{\nu} \cdot \nabla \theta_{ns})_k \quad (\text{B.6})$$

where ℓ_k and θ_k are the length and the value of θ at the midpoint of \mathcal{L}_k , respectively. On the other hand, $(\boldsymbol{\nu} \cdot \nabla \theta_{ns})_k$ is the value of the non-singular normal derivative obtained from Eq. (A.7). Finally, the last term in Eq. (B.2) can be obtained by standard integration techniques, where θ_{ns} in the branch cut is evaluated using Eq. (A.3).

Appendix C. Exact elastic contribution to the free energy density for the symmetric textures on crenellated substrates

In this Appendix we will evaluate the elastic free energy of the symmetric textures on a crenellated substrate characterized by a block of width l_1 and height h , and period $\lambda = l_1 + l_2$. We note that, due to the symmetry of the texture, we may evaluate the elastic free energy in the domain shown in Fig. 15(a), which corresponds to half a period of the substrate relief. The domain boundary follows the substrate except close to its cusps, where it is rounded by arcs of circle of radii ξ_0 . The vertical lateral sides run from the substrate to infinity. We set the origin on the lower substrate cusp, so the upper substrate cusp is at $(0, h)$. On the domain boundary we set $\theta = 0$ except for the vertical segment which joins the two surface cusps, where we set either $\theta = \pi/2$ or $\theta = -\pi/2$ (depending on the symmetric texture considered).

We map the domain in the z -plane to the upper half ζ -plane by using the following Schwarz-Christoffel transformation:

$$z = C \int \frac{\sqrt{\zeta + 1} d\zeta}{\sqrt{\zeta + a} \sqrt{\zeta} \sqrt{\zeta - b}} + C' \quad (\text{C.1})$$

$$= C' + \frac{2C}{\sqrt{a+b}} \left[(1+b) F \left(\gamma \middle| \frac{a(1+b)}{a+b} \right) - b \Pi \left(\frac{a}{a+b}; \gamma \middle| \frac{a(1+b)}{a+b} \right) \right] \quad (\text{C.2})$$

$$\text{with } \gamma = \arcsin \left[\text{sign} \left(\frac{\zeta}{\zeta - b} \right) \sqrt{\frac{(a+b)\zeta}{a(\zeta - b)}} \right]$$

where C and C' are complex constants, $a > 1$ and $b > 0$ real numbers, and $F(z|m)$ and $\Pi(n; z|m)$ are the incomplete elliptic integral of the first and third kind, respectively. The points $-l_1/2 + ih$, ih , 0 and $l_2/2$ in the z -plane are mapped onto $-a$, -1 , 0 and b , respectively. These conditions fix the values of C , C' , a and b . In particular, as $F(0|m) = \Pi(n; 0|m) = 0$, we find that $C' = 0$. On the other hand, the real part of Eq. (C.2) diverges as $\zeta \rightarrow \pm\infty$, but the imaginary parts have well defined values which differ by πC . Consequently, $C = i(l_1 + l_2)/2\pi$. Finally, the values of a and b are determined by the requirement that the image of the point $-l_1/2 + ih$ is $-a$ in the ζ -plane. This

leads to the conditions:

$$\frac{h}{l_1 + l_2} = \frac{1}{\pi\sqrt{a+b}} \Re \left[(1+b)K \left(\frac{a(1+b)}{a+b} \right) - b\Pi \left(\frac{a}{a+b} \middle| \frac{a(1+b)}{a+b} \right) \right] \quad (\text{C.3})$$

$$\frac{l_1}{l_1 + l_2} = \frac{2}{\pi\sqrt{a+b}} \Im \left[(1+b)K \left(\frac{a(1+b)}{a+b} \right) - b\Pi \left(\frac{a}{a+b} \middle| \frac{a(1+b)}{a+b} \right) \right] \quad (\text{C.4})$$

where $\Re(z)$ and $\Im(z)$ are the real and imaginary parts of z , respectively, and $K(m)$ and $\Pi(n|m)$ are the complete elliptic integrals of the first and third kinds, respectively. The values of a and b must be obtained numerically from these conditions for given values of $h/(l_1 + l_2)$ and $l_1/(l_1 + l_2)$.

In order to obtain the orientational field θ , we solve the Laplace equation in the upper half ζ -plane, with the real axis as boundary, except close to -1 and 0 , where it is rounded by arcs of circle of radii ϵ_1 and ϵ_2 , respectively. The boundary conditions are $\tilde{\theta} = 0$ for $\zeta < -1 - \epsilon_1$ and $\zeta > \epsilon_2$, and $\pm\pi/2$ for $-1 + \epsilon_1 \leq \zeta \leq -\epsilon_2$. The solution is:

$$\tilde{\theta}(\zeta) = \pm \frac{1}{2} \left[\arctan \left(\frac{\tilde{y}}{\tilde{x}} \right) - \arctan \left(\frac{\tilde{y}}{\tilde{x} + 1} \right) \right] \quad (\text{C.5})$$

where $\zeta = \tilde{x} + i\tilde{y}$. The orientational field in the original domain is $\theta(x, y) = \tilde{\theta}(\zeta(z))$, where $z = x + iy$. Thus the free energy per z -unit length and x -period is

$$\begin{aligned} K \int dx dy |\nabla\theta|^2 &= K \int d\tilde{x} d\tilde{y} |\nabla'\tilde{\theta}|^2 \\ &= \mp \frac{K\pi}{2} \int_{-1+\epsilon_1}^{-\epsilon_2} \left(\frac{\partial\tilde{\theta}}{\partial\tilde{y}} \right) d\tilde{x} = -\frac{K\pi}{4} \ln(\epsilon_1\epsilon_2) \end{aligned} \quad (\text{C.6})$$

We can use Eq. (C.1) to relate ϵ_1 and ϵ_2 to ξ_0 [32], leading to:

$$\epsilon_1 = \left(3\pi \frac{\xi_0}{l_1 + l_2} \sqrt{a-1} \sqrt{b+1} \right)^{2/3} \quad (\text{C.7})$$

$$\epsilon_2 = \left(\pi \frac{\xi_0}{l_1 + l_2} \sqrt{ab} \right)^2 \quad (\text{C.8})$$

Therefore, the free energy Eq. (C.6) can be recast as:

$$\frac{2\pi K}{3} \ln \frac{l_1 + l_2}{\xi_0} - \frac{K\pi}{6} \ln \left(3\pi^4 \sqrt{a-1} \sqrt{b+1} (ab)^{3/2} \right) \quad (\text{C.9})$$

Note that this expression depends only on the geometric characteristics of the surface relief, and not on the boundary condition which determines the symmetric nematic texture. Thus, both symmetric textures have exactly the same elastic contribution to the free energy. This is consistent with the results for the single step solution [42], which would correspond to our case in the limit $l_1 \rightarrow \infty$ and $l_2 \rightarrow \infty$.

References

- [1] Lee B-W and Clark N A 2001 *Science* **291** 2576
- [2] Kim J-H, Yoneya M and Yokoyama H 2002 *Nature* **420** 19.
- [3] Ferjani S, Choi Y, Pendery J, Petschek R G and Rosenblatt C 2010 *Phys. Rev. Lett.* **104** 257801.
- [4] Brown C V, Towler M J, Hui V C and Bryan-Brown G P 2000 *Liq. Cryst.* **27** 233.
- [5] Uche C, Elston S J and Parry-Jones L A 2005 *J. Phys. F: Appl. Phys.* **38** 2283.
- [6] Uche C, Elston S J and Parry-Jones L A 2006 *Liq. Cryst.* **33** 697.
- [7] Davidson A J, Brown C V, Mottram N J, Ladak S and Evans C R 2010 *Phys. Rev. E* **81** 051712.
- [8] Evans C R, Davidson A J, Brown C V and Mottram N J 2010 *J. Phys. D: Appl. Phys.* **43** 495105.
- [9] Dammone O J, Zacharoudiou I, Dullens R P A, Yeomans J M, Lettinga M P and Aarts D G A L 2012 *Phys. Rev. Lett.* **109** 108303.
- [10] Silvestre N M, Patrício P and Telo da Gama M M 2004 *Phys. Rev. E* **69** 061402.
- [11] Ohzono T and Fukuda J.-i. 2012 *Nat. Commun.* **3** 701.
- [12] Silvestre N M, Liu Q, Senyuk B, Smalyukh I I and Tasinkevych M 2014 *Phys. Rev. Lett.* **112** 225501.
- [13] Eskandari Z, Silvestre N M, Telo da Gama M M and Ejtehadi M R 2014 *Soft Matter* **10** 9681.
- [14] Luo Y, Serra F, Beller D A, Gharbi M A, Li N, Yang S, Kamien R D and Stebe K J 2016 *Phys. Rev. E* **93** 032705.
- [15] Berreman D W 1972 *Phys. Rev. Lett.* **28** 1683
- [16] de Gennes P G and Prost J 1993 *The Physics of Liquid Crystals* (Oxford: Clarendon Press).
- [17] Barbero G 1980 *Lett. Nuovo Cimento Soc. Ital. Fis.* **29** 553.
- [18] Barbero G 1981 *Lett. Nuovo Cimento Soc. Ital. Fis.* **32** 60.
- [19] Barbero G 1982 *Lett. Nuovo Cimento Soc. Ital. Fis.* **34** 173.
- [20] Kitson S and Geisow A 2002 *Appl. Phys. Lett.* **80** 3635.
- [21] Fukuda J I, Yoneya M and Yokoyama H 2007 *Phys. Rev. Lett.* **98** 187803.
- [22] Kondrat S and Poniewierski A 2001 *Phys. Rev. E* **64** 031709.
- [23] Patrício P, Telo da Gama M M and Dietrich S. 2002 *Phys. Rev. Lett.* **88** 245502
- [24] Harnau L, Kondrat S and Poniewierski A 2005 *Phys. Rev. E* **72** 011701.
- [25] Kondrat S, Poniewierski A and Harnau L 2005 *Liq. Cryst.* **32** 95.
- [26] Harnau L and Dietrich S 2006 *Europhys. Lett.* **73** 28.
- [27] Harnau L, Kondrat S and Poniewierski A 2007 *Phys. Rev. E* **76** 051701.
- [28] Barbero G, Gliozzi A S, Scalendari M and Evangelista L R 2008 *Phys. Rev. E* **77** 051703.
- [29] Yi Y, Lombardo G, Ashby N, Barberi R, MacLennan J E and Clark N E 2009 *Phys. Rev. E* **79** 041701.
- [30] Poniewierski A 2010 *Eur. Phys. J. E* **31** 169.
- [31] Romero-Enrique J M, Pham C T and Patrício P 2010 *Phys. Rev. E* **82** 011707
- [32] Rojas-Gómez O A and Romero-Enrique J M 2012 *Phys. Rev. E* **86** 041706
- [33] Raisch A and Majumdar A 2014 *EPL* **107** 16002.
- [34] Ledney M F, Tarnavskyy O S, Lesiuk A I and Reshetnyak V Y 2016 *Liq. Cryst.* doi:10.1080/02678292.2016.1197973 .
- [35] Bramble J P, Evans S D, Henderson J R, Anquetil C, Cleaver D J and Smith N J 2007 *Liq. Cryst.* **34** 1059.
- [36] Patrício P, Pham C T and Romero-Enrique J M 2008 *Eur. Phys. J. E* **26** 97
- [37] Patrício P, Romero-Enrique J M, Silvestre N M, Bernardino N R and Telo da Gama M M 2011 *Mol. Phys.* **109** 1067
- [38] Patrício P, Silvestre N M, Pham C T and Romero-Enrique J M 2011 *Phys. Rev. E* **84** 021701
- [39] Patrício P, Tasinkevych M and Telo da Gama M M 2002 *Eur. Phys. J. E* **7** 117
- [40] Silvestre N M, Eskandari Z, Patrício P, Romero-Enrique J M and Telo da Gama M M 2012 *Phys. Rev. E* **86** 011703
- [41] Lewis A H, Garlea I, Alvarado J, Dammone O J, Howell P D, Majumdar A, Mulder B M, Lettinga

- M P, Koenderink G H and Aarts D G A L 2014 *Soft Matter* **10** 7865.
- [42] Davidson A J and Mottram N J 2012 *Eur. J. Appl. Math.* **23** 99
- [43] Oseen H 1933 *J. Chem. Soc. Faraday Trans. II* **29** 883.
- [44] Frank F C 1958 *Disc. Faraday Soc.* **25** 19.
- [45] Rapini A and Papoular M 1969 *J. Phys. (Paris) Colloq.* **30** C4-54.
- [46] Brebbia C A and Domínguez J 1992 *Boundary elements: an introductory course, 2nd ed.* (Southampton: Computational Mechanics Publications).
- [47] Katsikadelis J T 2002 *Boundary Elements: Theory and Applications* (Amsterdam: Elsevier).
- [48] Silvestre N M, Romero-Enrique J M and Telo da Gama M M 2016 *accepted in J. Phys: Condens. Matter*
- [49] Jeong J, Kang L, Davidson Z S, Collings P J, Lubensky T C and Yodh A G 2015 *Proc. Natl. Acad. Sci. USA* **112** E1837
- [50] Davidson Z S, Kang L, Jeong J, Still T, Collings P J, Lubensky T C and Yodh A G 2015 *Phys. Rev. E* **91** 050501(R)
- [51] Nayani K, Chang R, Fu J X, Ellis P W, Fernandez-Nieves A, Park J O and Srinivasarao M 2015 *Nature Commun.* **6** 8067

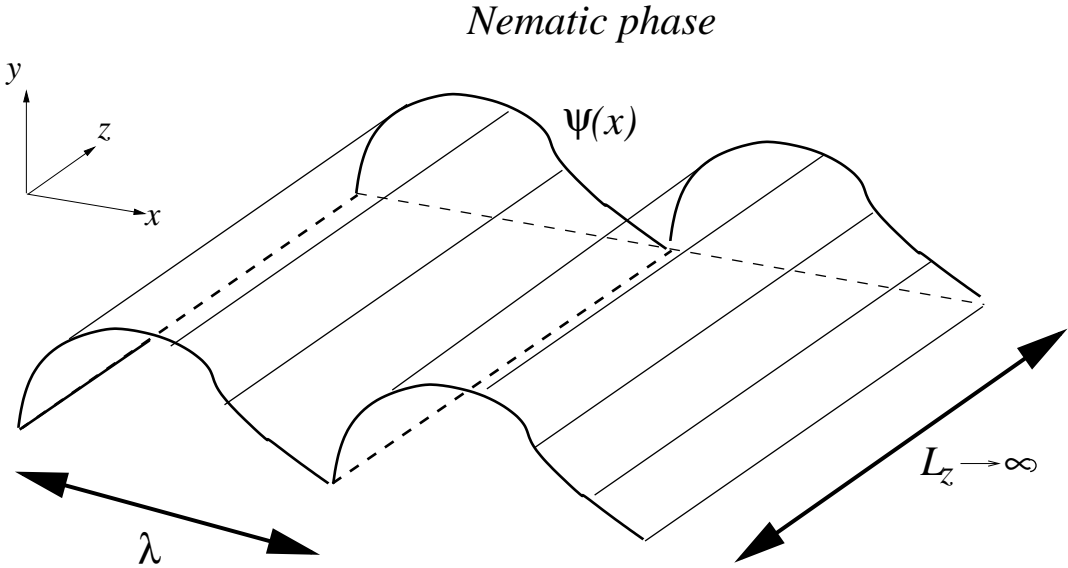


Figure 1. Schematic picture of the substrate geometry, characterized by the wavenumber λ and the relief profile $\psi(x)$.

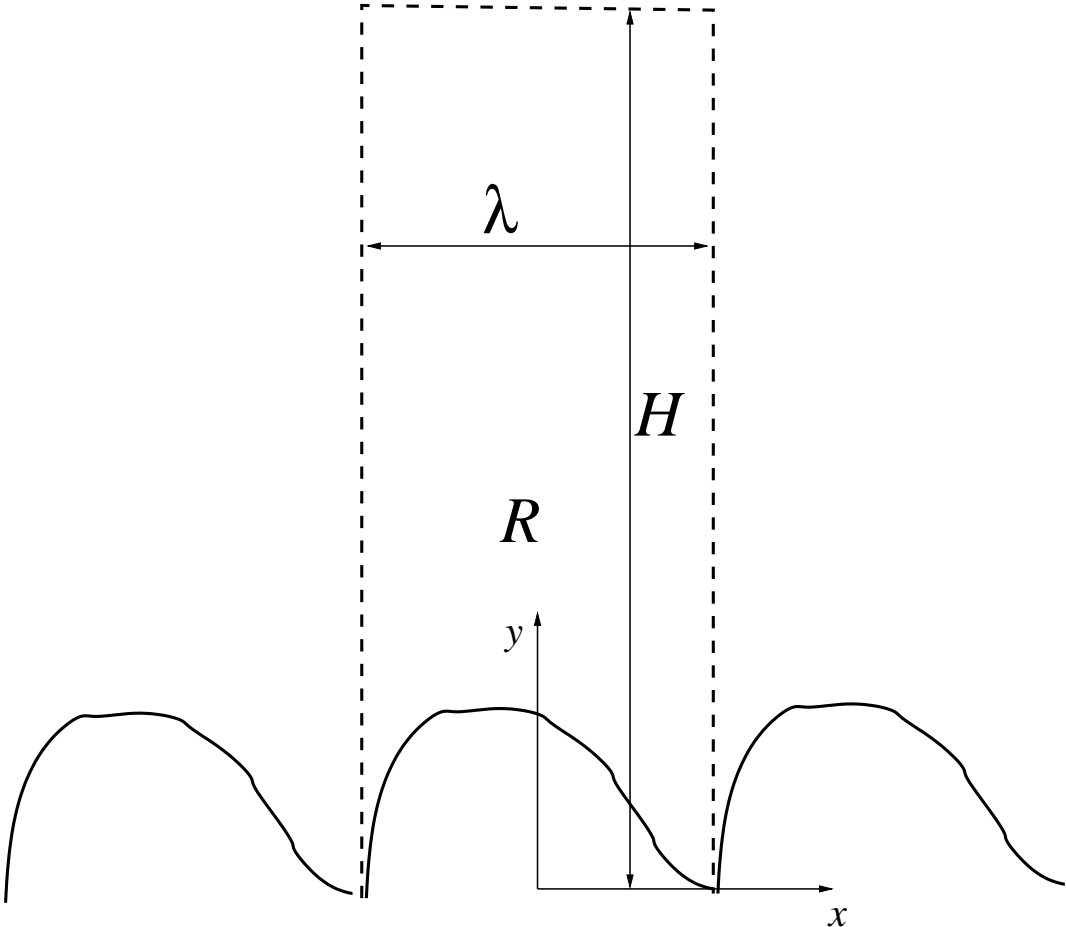


Figure 2. Plot of the region R where the equation for the orientational field θ is solved. λ is the period of the substrate relief and H is the height of the domain.

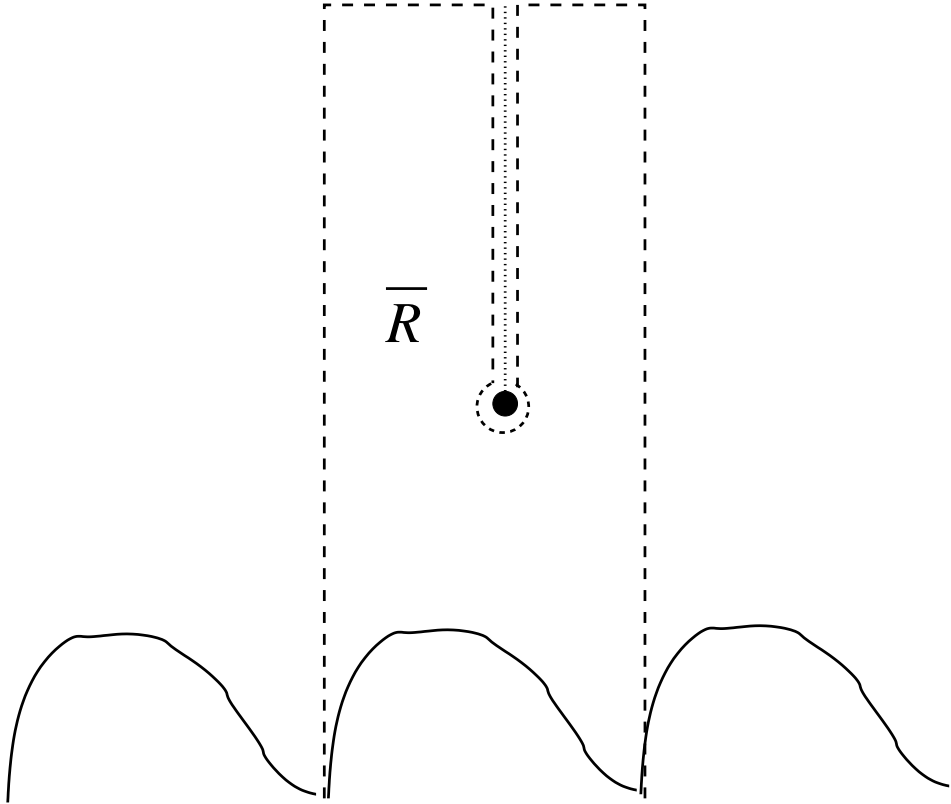


Figure 3. Plot of the modified region \bar{R} for a nematic with a $\pm 1/2$ -disclination line in the bulk, represented by the filled circle. The vertical dotted line corresponds to the branch cut, where a discontinuity of $\pm\pi$ in the orientational field is observed. The dashed line corresponds to the boundary of \bar{R} .

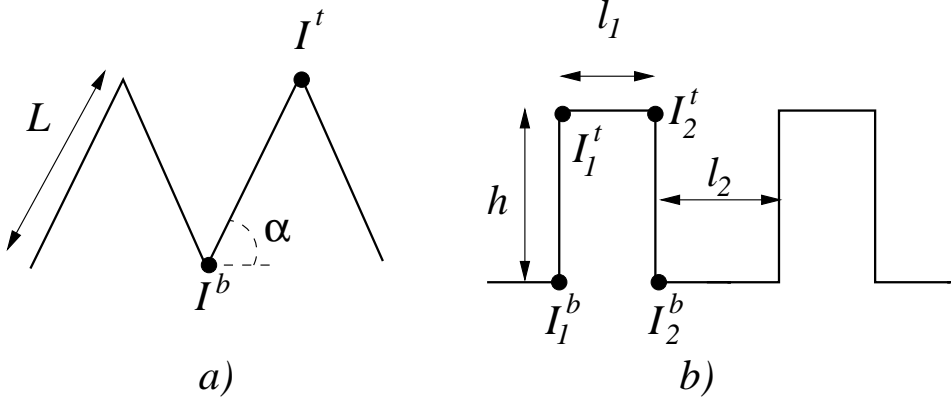


Figure 4. Geometric characteristics of: (a) a sawtooth substrate; (b) a crenellated substrate. The positions and effective topological charges I associated to the cusps of one substrate relief period are highlighted.

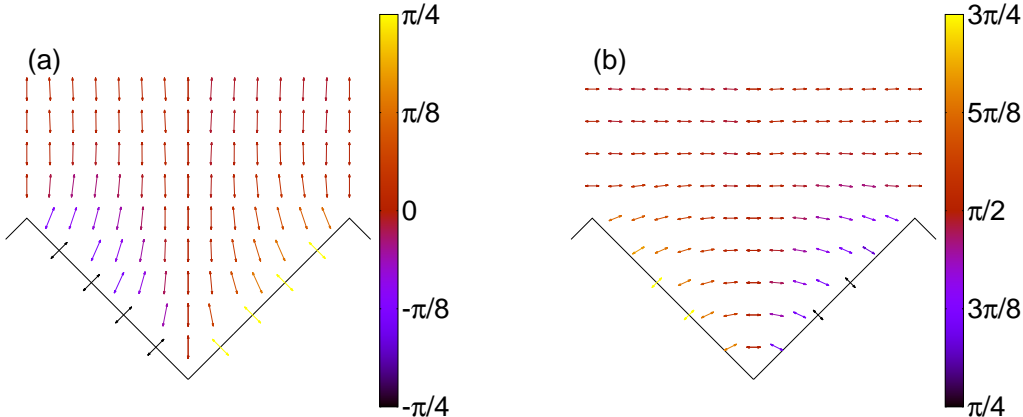


Figure 5. Coexisting textures at a sawtooth substrate ($\alpha = \pi/4$): (a) N^\perp texture, (b) N^\parallel texture. The arrows denote the local nematic director orientation and the colour code gives the orientational field θ .

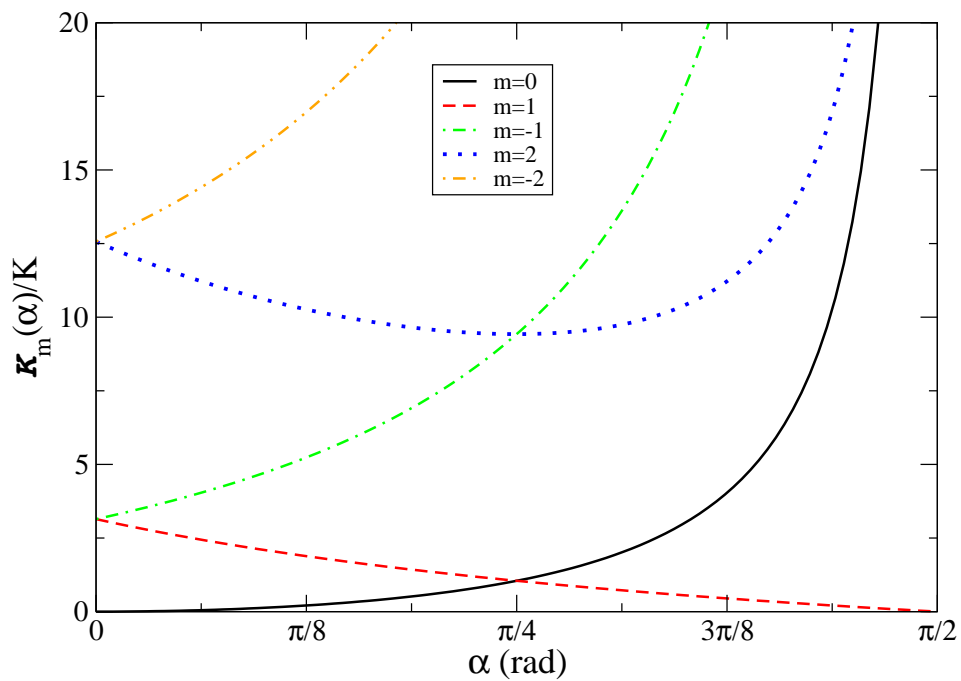


Figure 6. Plot of \mathcal{K}_m/K as a function of α for different values of m : $m = 0$ (continuous line), $m = +1$ (dashed line), $m = -1$ (dot-dashed line), $m = +2$ (dotted line) and $m = -2$ (double dot-dashed line).

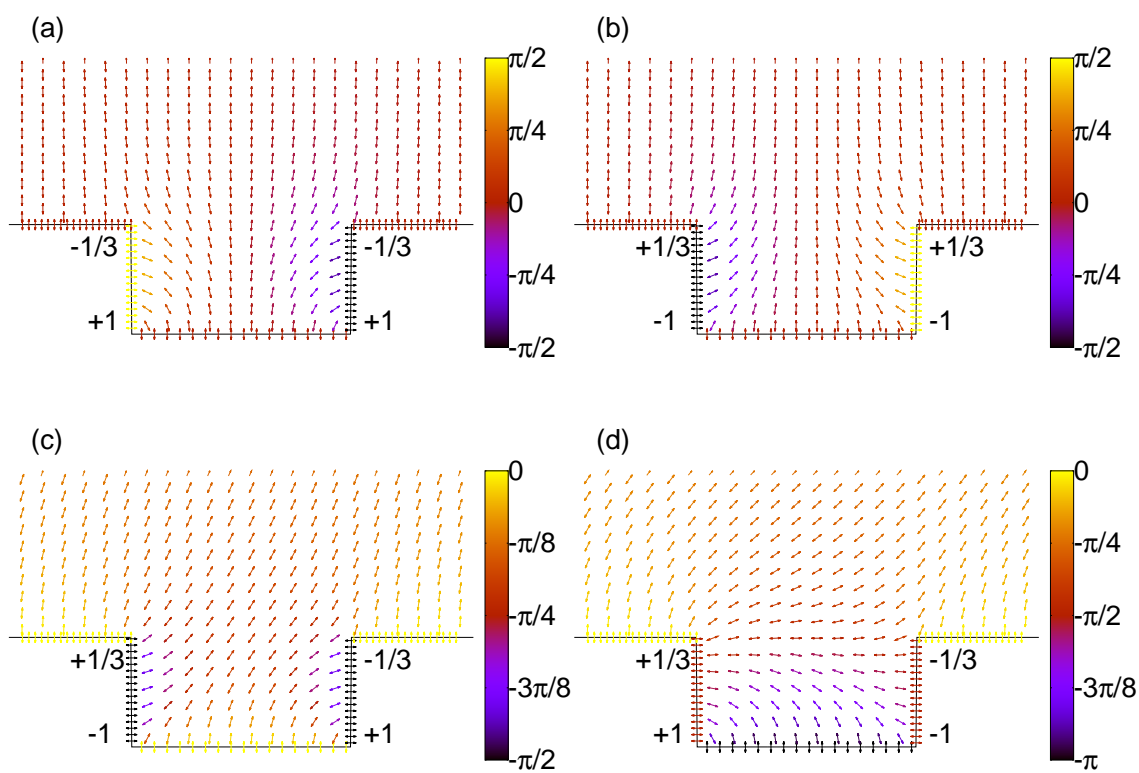


Figure 7. Typical textures at a crenellated substrate ($h/l_2 = 0.5$, $l_1/l_2 = 1$): (a) N_1^\perp texture, (b) N_2^\perp texture, (c) N_1^o texture and N_2^o texture. The meaning of the symbols is the same as in Fig. 5.

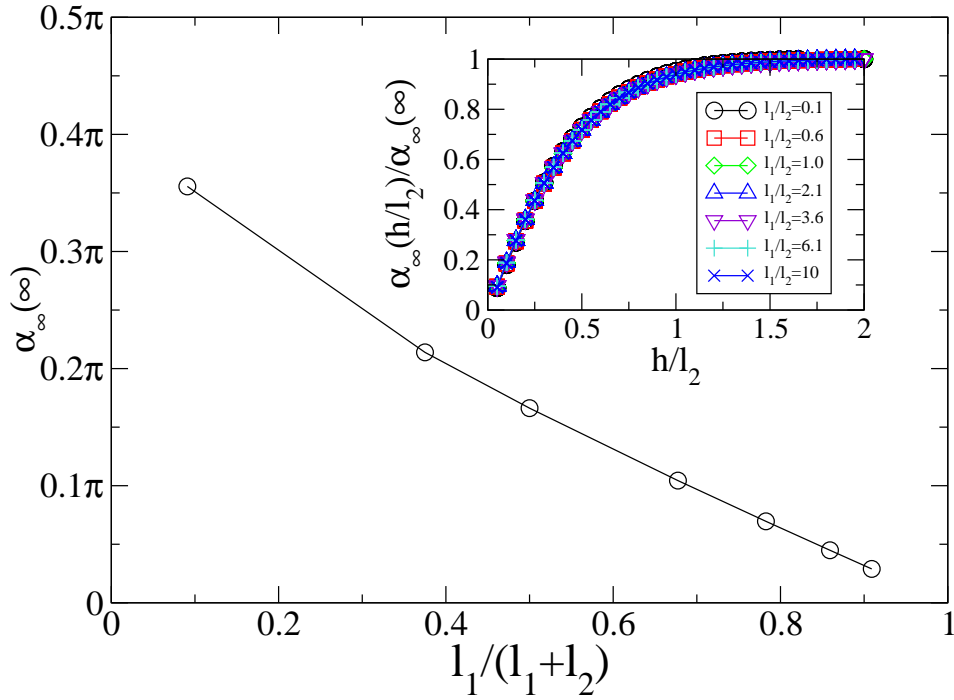


Figure 8. Plot of the asymptotic far-field orientation $\alpha_\infty(h/l_2 \rightarrow \infty)$ as a function of l_1/l_2 . Inset: plot of the ratio $\alpha_\infty(h/l_2; l_1/l_2)/\alpha_\infty(\infty; l_1/l_2)$ as a function of h/l_2 for $l_1/l_2 = 0.1$ (circles), 0.6 (squares), 1.0 (diamonds), 2.1 (triangles up), 3.6 (triangles down), 6.1 (pluses) and 10 (crosses).

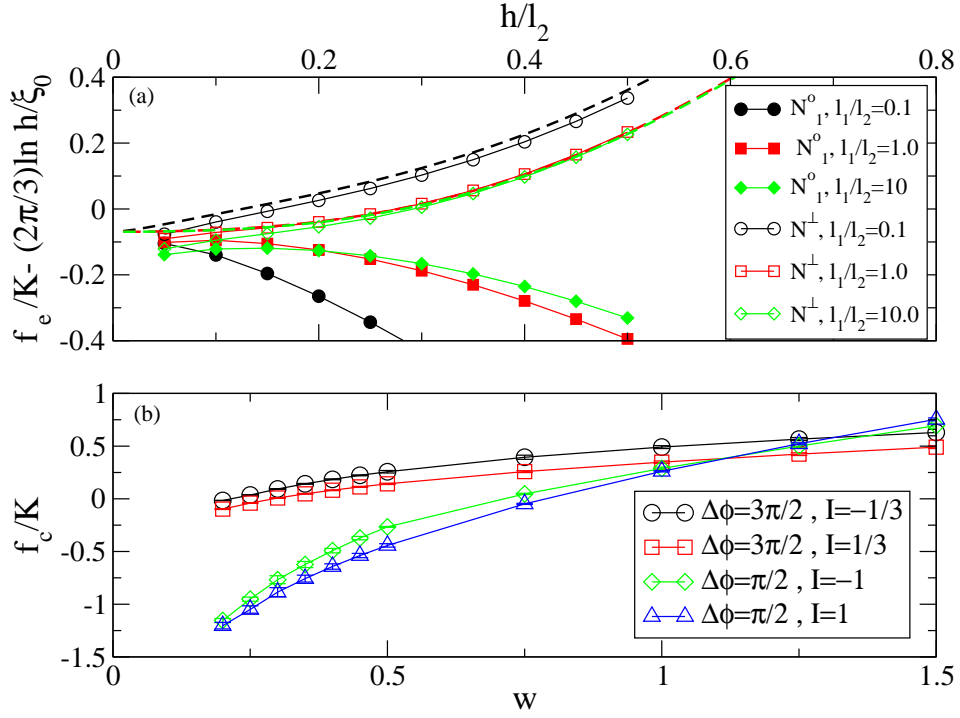


Figure 9. Top panel: Plot of the next-to-leading elastic contribution to the interfacial free energy with respect to h/l_2 corresponding to the N_i^\perp (open symbols) and N_1^o (filled symbols) for $l_1/l_2 = 0.1$ (circles), 1 (squares) and 10 (diamonds). Dashed lines correspond to the analytical prediction Eq. (C.9). Bottom panel: plot of the core contributions as a function of the anchoring parameter w for the cusps with opening angle $\Delta\phi$ and topological charge: $\Delta\phi = 3\pi/2$ and $I = -1/3$ (circles), $\Delta\phi = 3\pi/2$ and $I = +1/3$ (squares), $\Delta\phi = \pi/2$ and $I = -1$ (diamonds) and $\Delta\phi = \pi/2$ and $I = 1$ (triangles).

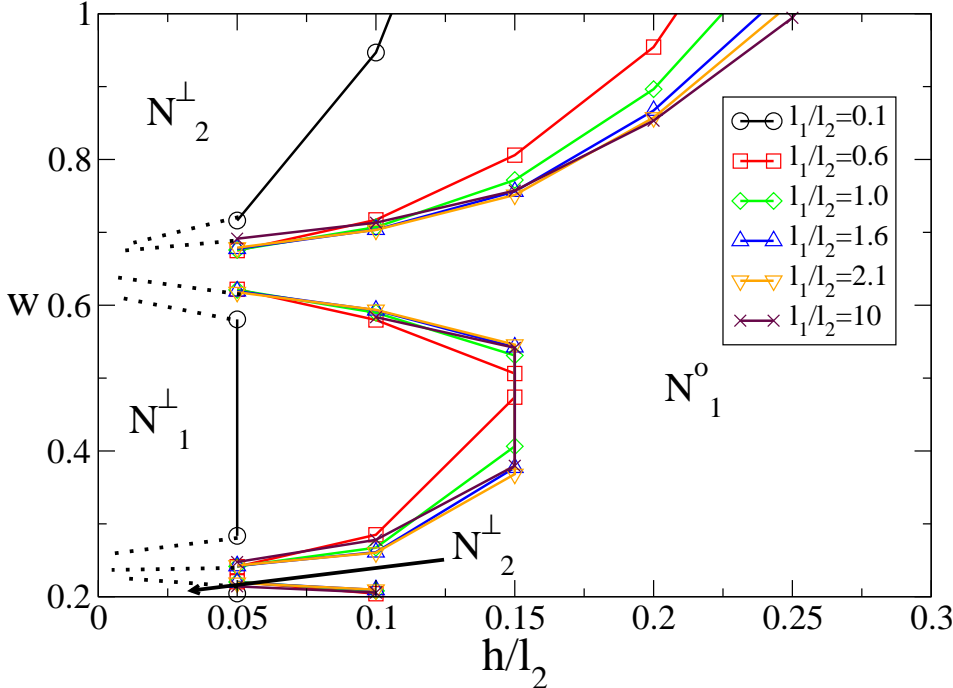


Figure 10. Phase diagram for the crenellated substrate in terms of h/l_2 and the anchoring parameter w for $l_1/l_2 = 0.1$ (circles), 0.6 (squares), 1.0 (diamonds), 1.6 (up-triangles), 2.1 (down triangles) and 10.0 (crosses). The lines are a guide to the eye, with the dotted lines illustrating the continuation of coexistence at small h .

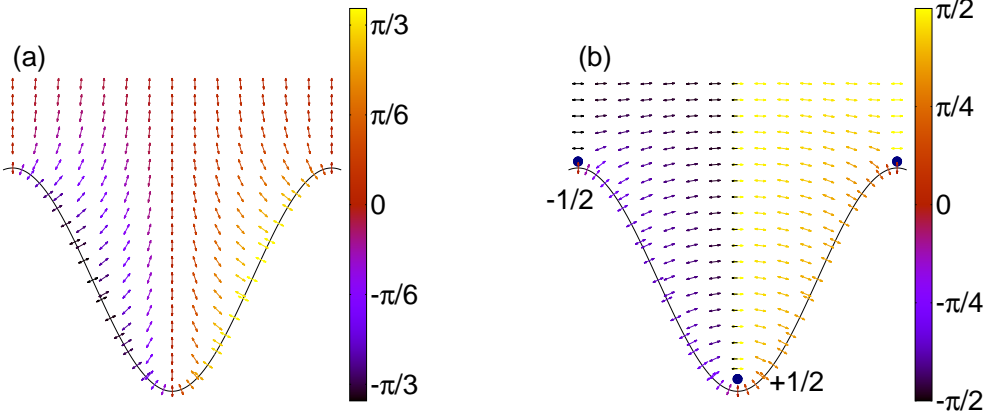


Figure 11. Typical textures at a sinusoidal substrate ($A/\lambda = 0.35$): (a) N^\perp texture, (b) N^\parallel texture. In the latter, the position of the disclination lines in the nematic are highlighted. The meaning of the symbols is the same as in Fig. 5.

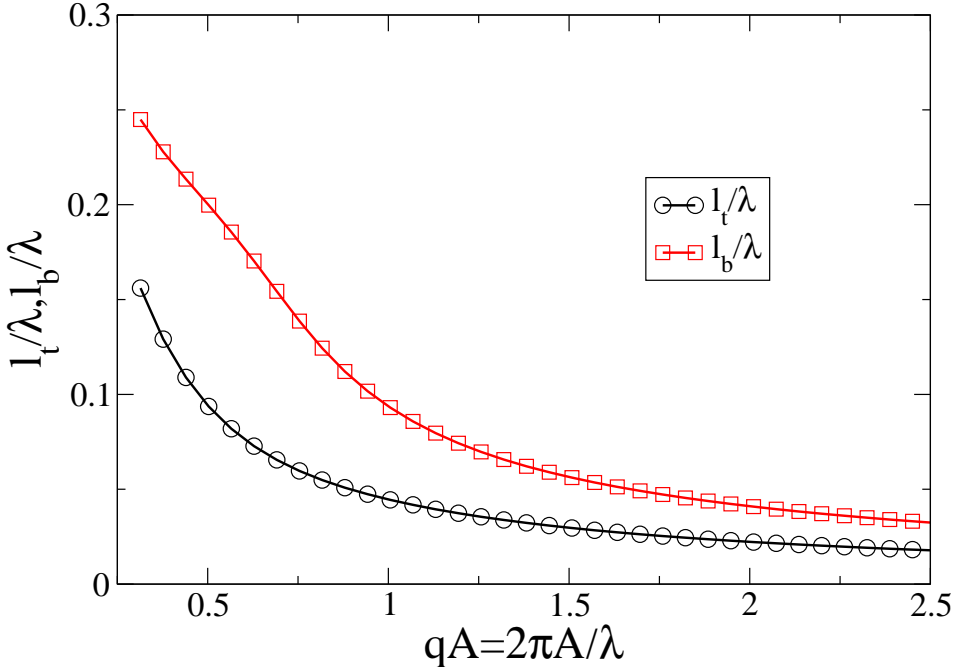


Figure 12. Distance with respect to the substrate of the top and bottom disclination lines, l_t and l_b , respectively, as a function of qA .

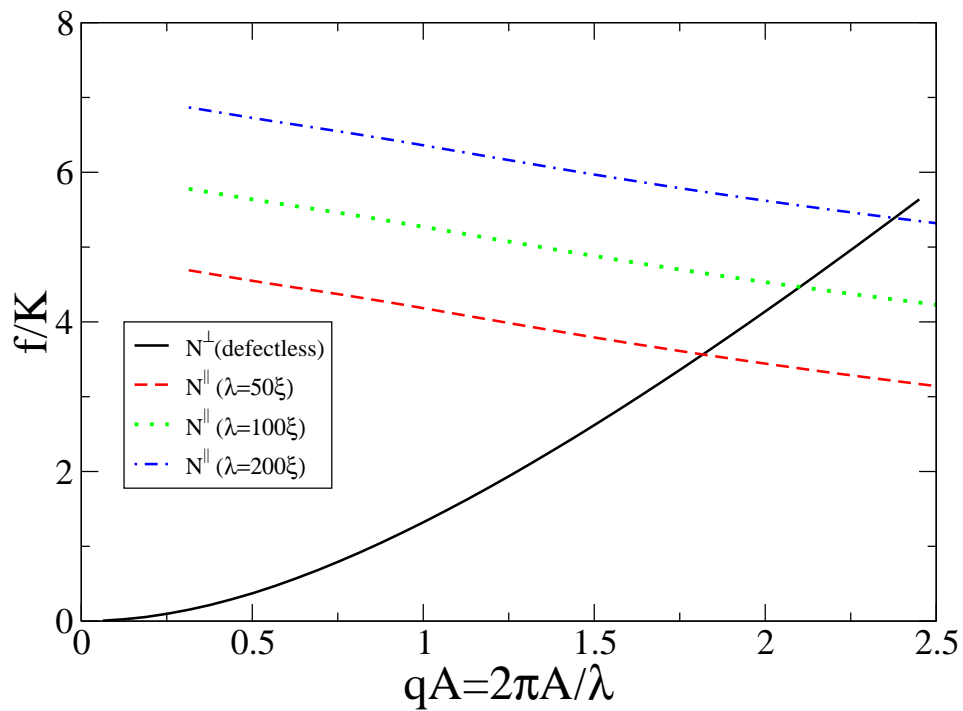


Figure 13. Free energy of the N^\perp (continuous line) and N^\parallel textures with $\lambda/\xi_0 = 50$ (dashed line), 100 (dotted line) and 200 (dot-dashed line).

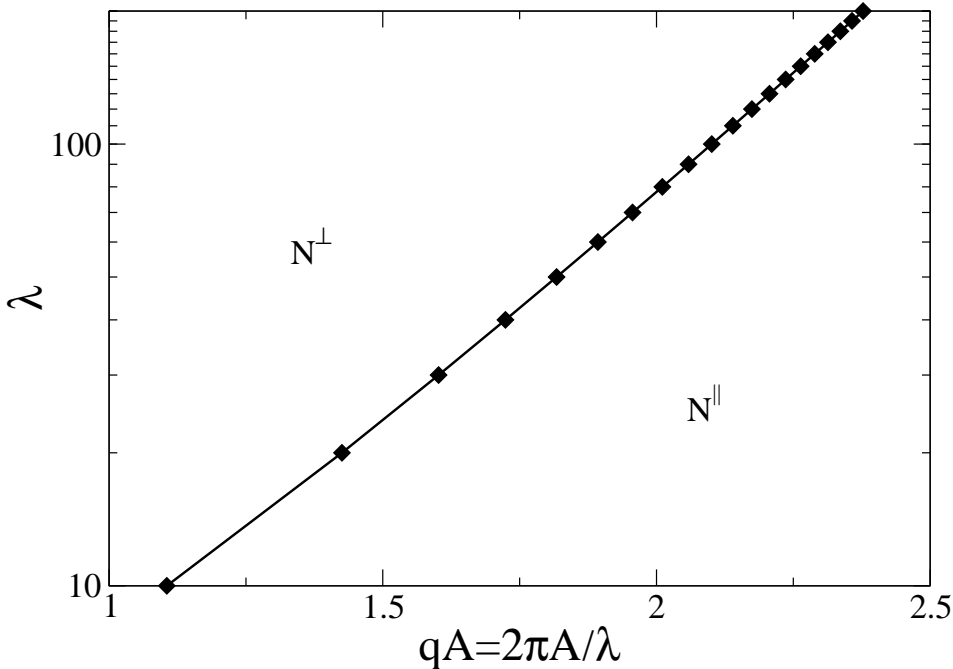


Figure 14. Phase diagram for the crenellated substrate in terms of the roughness parameter qA and the substrate period λ .

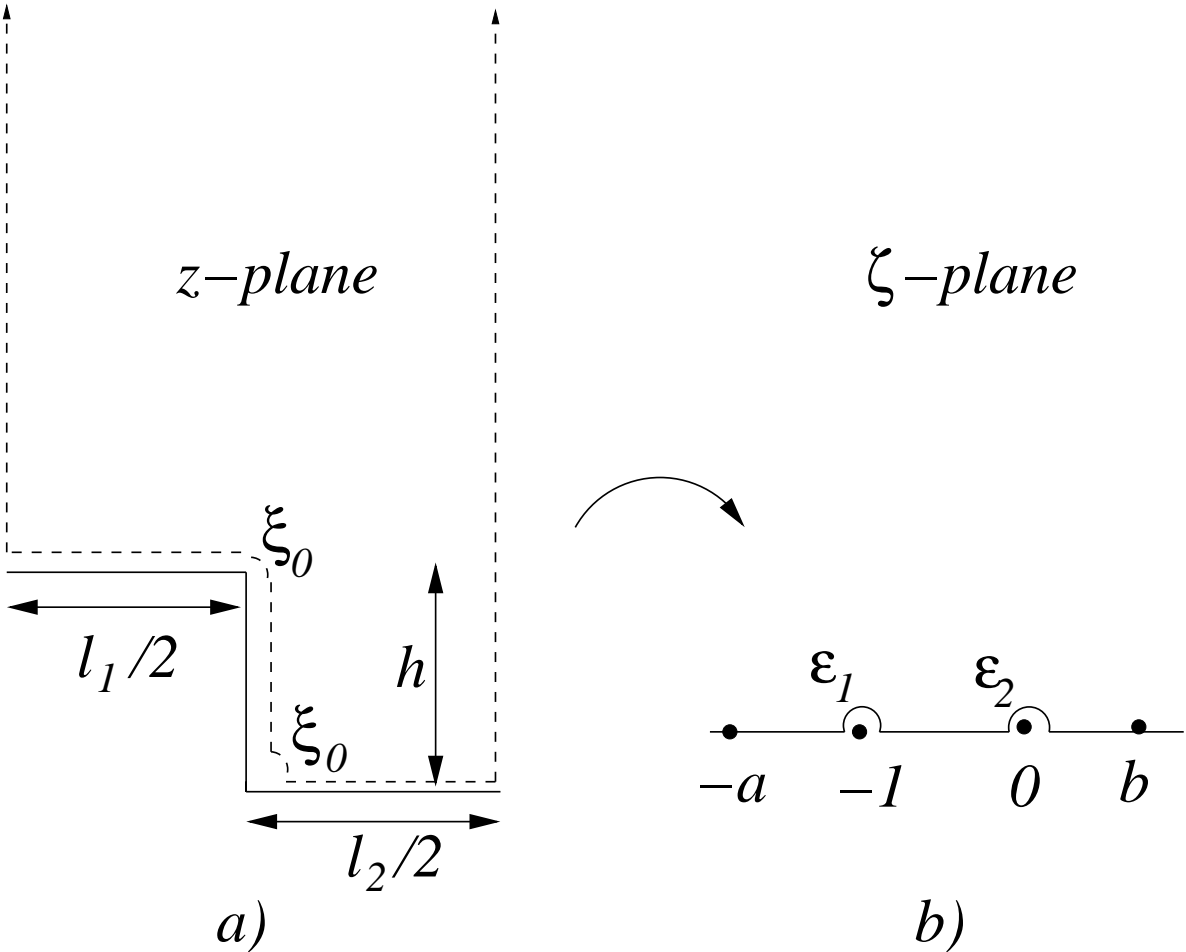


Figure 15. Left panel: Minimization cell for the evaluation of the elastic free energy. The solid line corresponds to the substrate, and the dashed line to the boundary of the domain where the orientation field θ is calculated. Right panel: Mapping of the minimization cell under the Schwarz-Christoffel transformation.